S1 Attached data

A folder is attached with modeled snowflake backscatter cross sections and dual-wavelength ratios of snowfall equivalent radar reflectivity factors for representing individual snowflakes by collections of randomly distributed ice spheres, as described and discussed in the main text. Data are given as .txt files. See README file and comment lines in data files for details.

S2 Additional figures

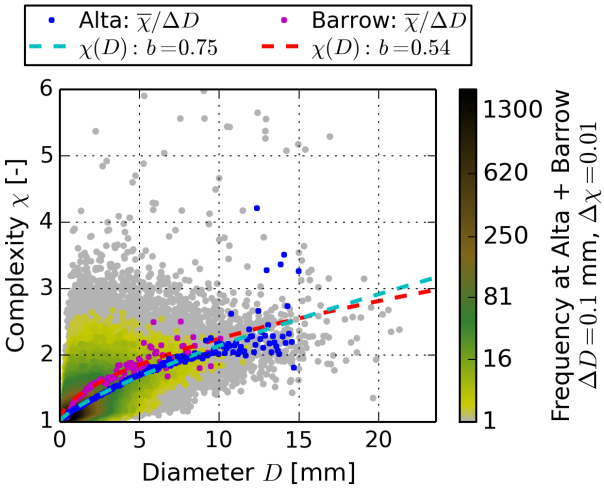

Figure S1. Non-logarithmic version of Fig. 3: 2D histogram of snowflake diameter D and complexity χ for bin sizes of $\Delta D = 0.1$ mm, $\Delta\chi = 0.01$. Mean complexity values per size bin are indicated by $\overline{\chi}/\Delta D$ for snowflake data collected at Alta and at Barrow separately. Snowflake complexity–diameter relationships $\chi(D)$ for the data sets collected at Alta and at Barrow are determined by the non-linear least squares method for fitting Eq. (2) to the values of $\overline{\chi}/\Delta D$ and characterized by the power-law exponent b.

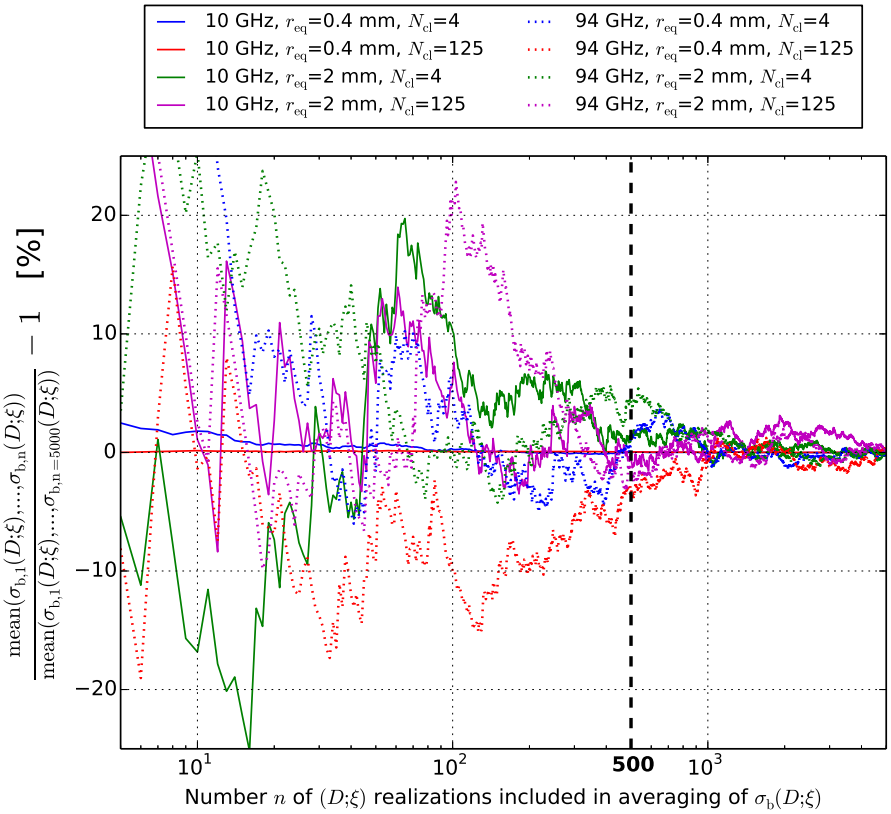

Figure S2. Impact of the number n of realizations of random ice sphere collections on the average backscatter cross section $\sigma_{\mathrm{b}}(D;\xi) = \mathrm{mean}(\sigma_{\mathrm{b},1}(D;\xi),...,\sigma_{\mathrm{b},n}(D;\xi))$ for a given $(D;\xi)$ configuration. Here, ice sphere collections are specified by the respective (single) mass-equivalent ice sphere radius r_{eq} and by the number $N_{\mathrm{cl}} = \xi^3$ of constituent ice spheres. Calculated percent differences of the average values of $\sigma_{\mathrm{b}}(D;\xi)$ are shown at frequencies of 10 and 94 GHz, i.e., at the lowest and the highest frequency included in the analysis.

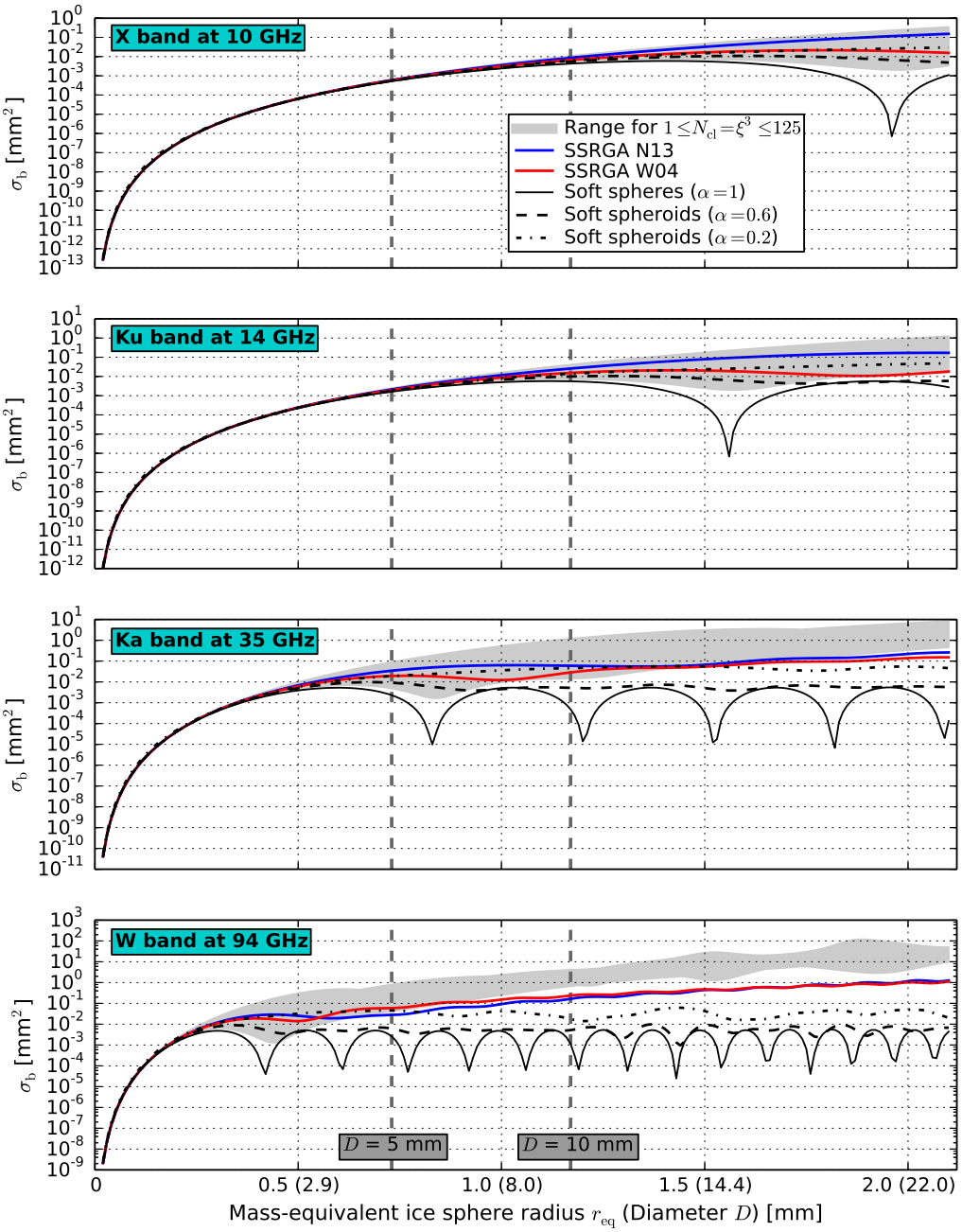

Figure S3. Modeled snowflake backscatter cross sections σ_b for collections of $1 \leq N_{cl} \leq 125$ randomly distributed ice spheres inside a spherical bounding volume of diameter D, corresponding to normalized surface-area-to-volume ratios of $1 \leq \xi \leq 5$; for the self-similar Rayleigh–Gans approximation (SSRGA) applied to N13 and to W04 aggregate snowflakes following the parameterizations given by Hogan et al. (2017); and for soft spheres and oblate spheroids with aspect ratios of $\alpha = 1$ and $\alpha = 0.6$ and 0.2, respectively.

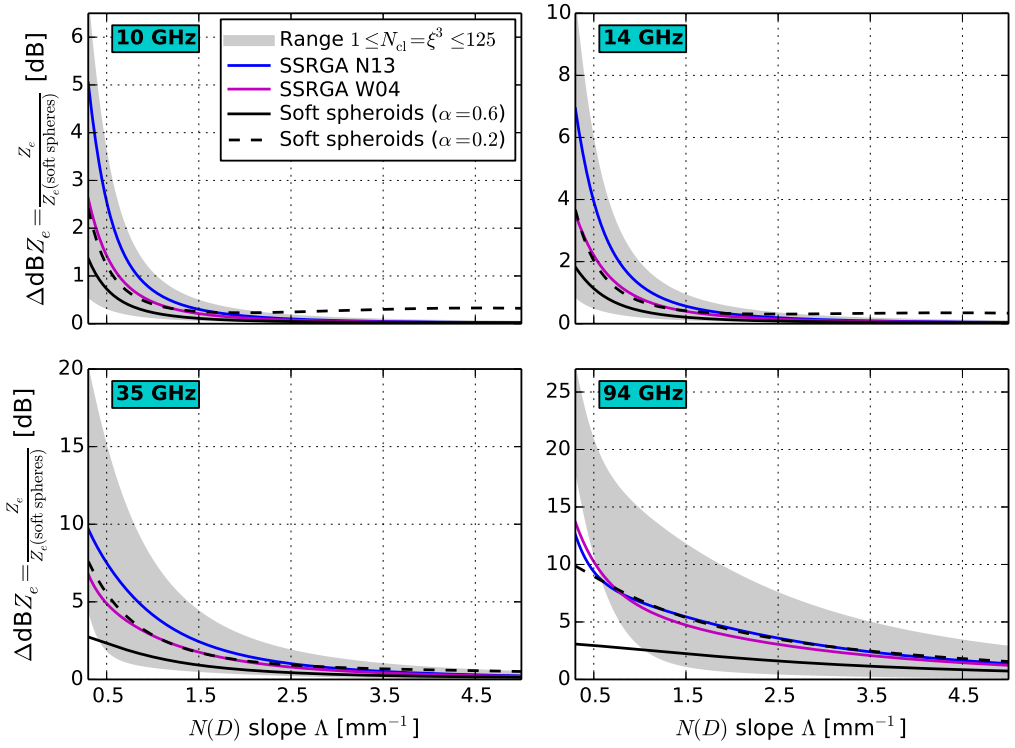

Figure S4. Overview of modeled snowfall (equivalent) radar reflectivity factors Z_e based on the backscatter cross sections shown in Fig. S3 and for exponential size distributions $N(D)$ with exponential slope parameters of $0.3 \leq \Lambda \leq 5.0$ mm^{-1} according to Eq. (1). Modeled Z_e are given as ratio relative to the Z_e value calculated for the corresponding size distribution of soft spheres and in units of dB, equivalent to dBZ_e differences indicated as ΔdBZ_e. Presented Z_e ratios and dBZ_e differences are independent of the constant scaling factor N_0 in Eq. (1).

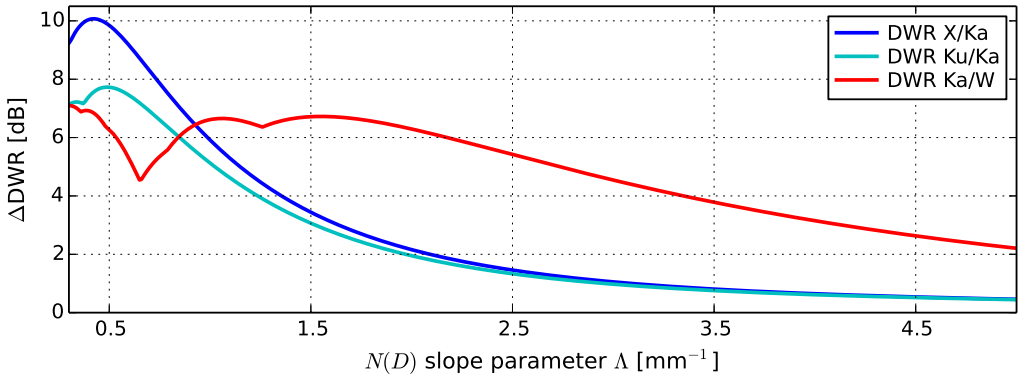

Figure S5. Impact of normalized surface-area-to-volume ratio ξ on dual-wavelength ratios (DWRs) of modeled snowfall radar reflectivity factors for exponential size distributions $N(D)$ with snowflake diameters of $D \leq 23.6$ mm and exponential slope parameters of $0.3 \leq \Lambda \leq 5.0$ mm^{-1}. Shown ΔDWR curves indicate the maximum difference in derived DWRs in Fig. 7 that is associated with the range of $1 \leq \xi \leq 5$, corresponding to collections of $1 \leq N_{\mathrm{cl}} \leq 125$ randomly distributed ice spheres inside the spherical snowflake bounding volume.

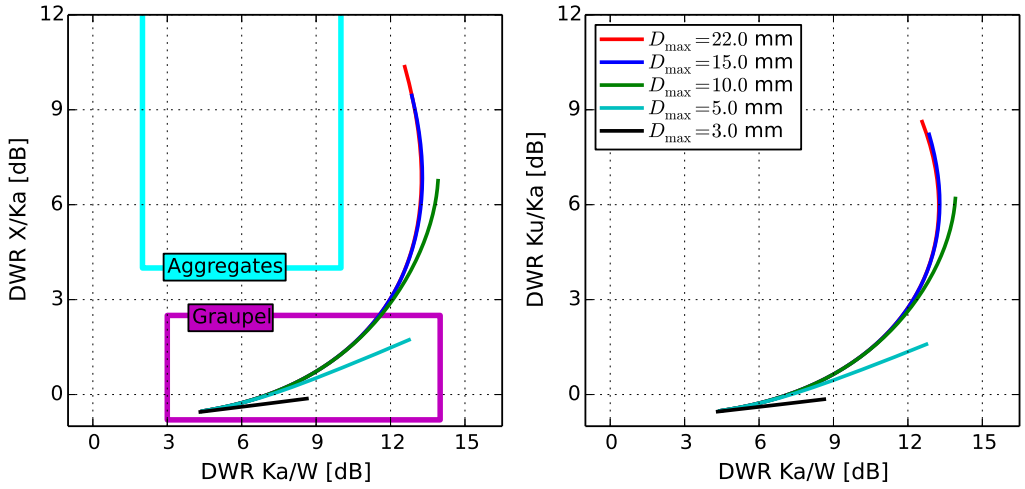

Figure S6. Snowfall triple-frequency curves determined for the 3D shape models of strongly rimed snowflakes presented by Leinonen and Szyrmer (2015) according to their riming model B and for an effective liquid water path of 1 kg m^{-2}. The triple-frequency radar signatures were derived for exponential size distributions characterized by snowflake diameters of $D \leq D_{\max}$ and exponential slope parameters of $0.3 \leq \Lambda \leq 5.0$ mm^{-1}. As in Fig. 7, colored rectangles are adapted from Kneifel et al. (2015) and roughly outline regions associated with the presence of large aggregate snowflakes (cyan) and rimed snowflakes (graupel; magenta), inferred by relating snowfall triple-frequency radar reflectivity measurements at X, Ka, and W band to coincident in situ snowflake observations. Snowflake size distributions truncated at smaller $D_{\max}$ yield flatter triple-frequency curves. This flattening effect leads to modeled triple-frequency curves (here illustrated for $D_{\max} = 5.0$ and 3.0 mm) within the range of triple-frequency radar signatures related to snowflake riming by Kneifel et al. (2015). Not included in the derivation of the shown triple-frequency curves are backscatter cross sections of small snowflakes with $D < 1.5$ mm that were calculated by Leinonen and Szyrmer (2015) for soft spheroids characterized by the radius of gyration. A comparison of the shown curves for $D_{\max} = 22.0$ mm with the corresponding triple-frequency curves of Leinonen and Szyrmer (2015) indicates that ignoring snowflakes with $D < 1.5$ mm cuts off low DWR Ka/W < 4.5 dB and slightly shifts the curves toward lower DWR X/Ka and DWR Ku/Ka by 1–2 dB. The overall trend of flatter modeled triple-frequency curves for snowflake size distributions truncated at smaller $D_{\max}$, however, does not depend on whether soft spheroids with $D < 1.5$ mm are included in the analysis or ignored.

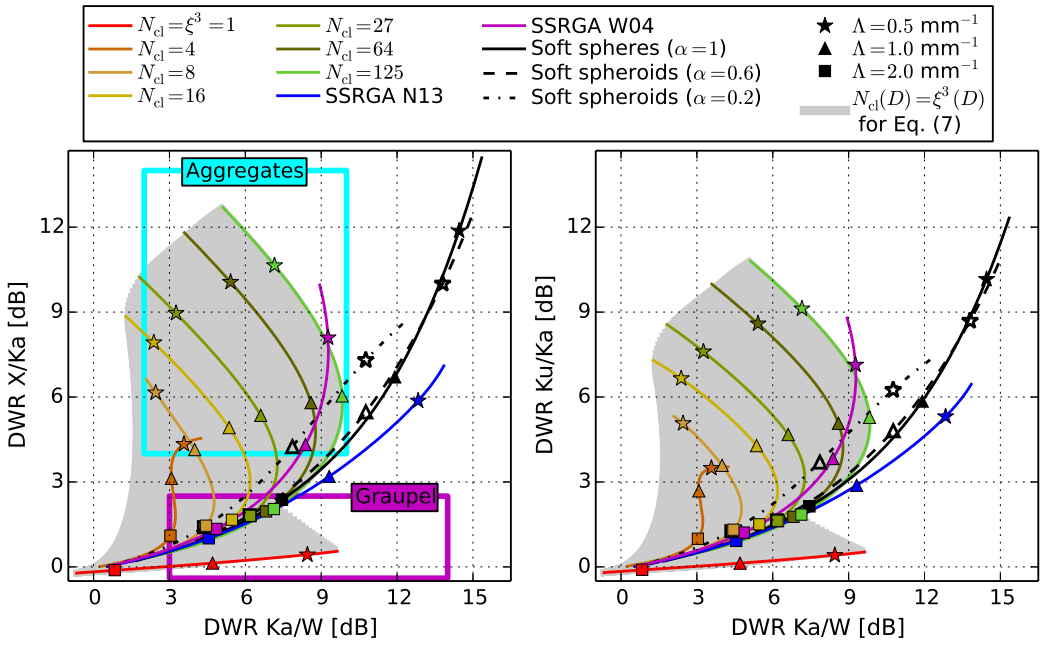

Figure S7. Modeled snowfall triple-frequency radar signatures as in Fig. 7, but derived for exponential size distributions limited to snowflake diameters of $D \leq D_{\max} = 10.0$ mm.

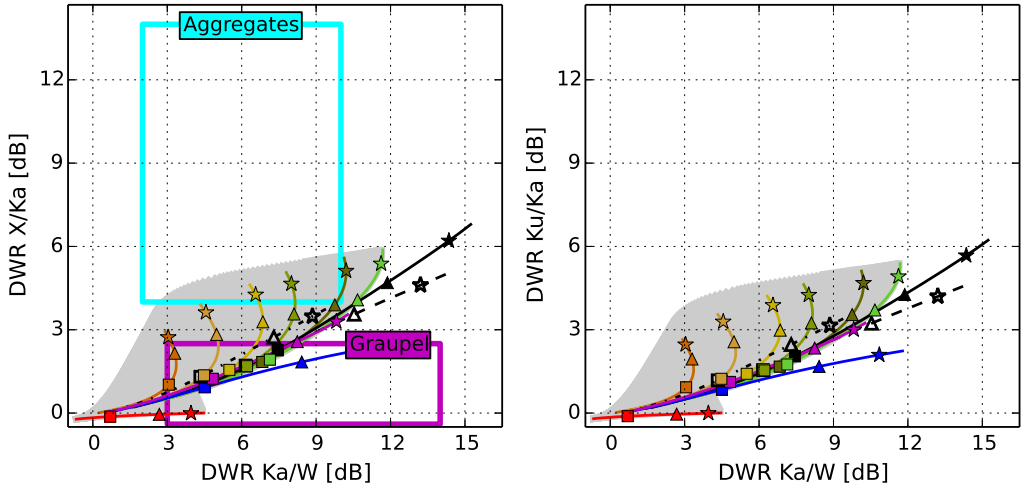

Figure S8. Modeled snowfall triple-frequency radar signatures as in Fig. S7, but derived for exponential size distributions limited to snowflake diameters of $D \leq D_{\max} = 5.0$ mm.

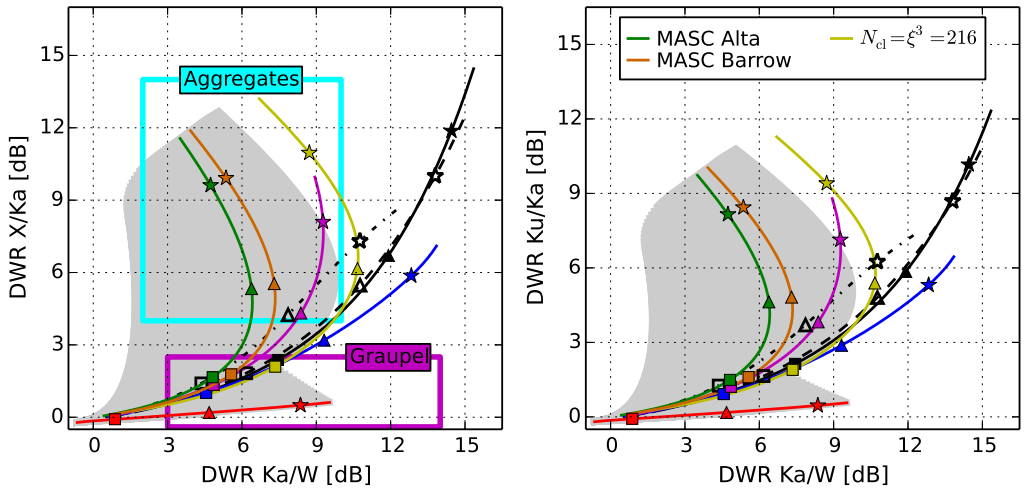

Figure S9. Modeled snowfall triple-frequency radar signatures as in Fig. 8, but derived for exponential size distributions limited to snowflake diameters of $D \leq D_{max} = 10.0$ mm.

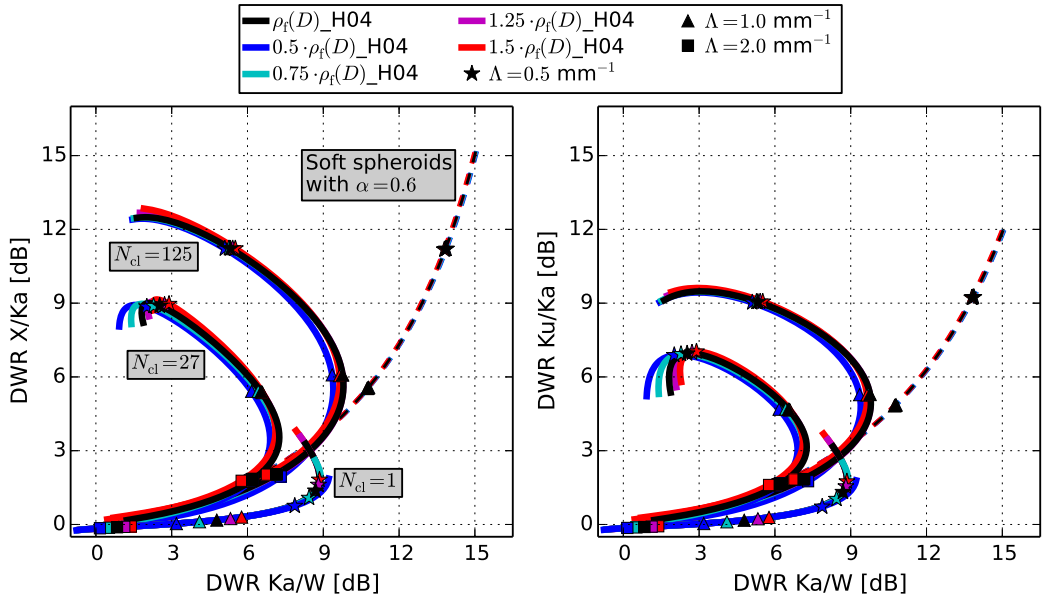

Figure S10. Impact of the parameterization of snowflake mass on modeled snowfall triple-frequency radar signatures for exponential size distributions with snowflake diameters of $D \leq D_{max} = 23.6$ mm and exponential slope parameters of $0.3 \leq \Lambda \leq 5.0$ mm^{-1}. In this study, snowflake density $\rho_f(D)$ and mass $m_f(D)$ are calculated from snowflake diameter D according to Heymsfield et al. (2004), indicated as $\rho_f(D)$_H04. The impact of the parameterization of snowflake mass on modeled snowfall radar signatures is evaluated by uniformly increasing and decreasing $\rho_f(D)$_H04, and thus $m_f(D)$ given by Eqs. (3) and (4), by 25 % and by 50 %. Modeling results for collections of $N_{cl} = 1,\ 27,\ 125$ randomly distributed ice spheres inside the spherical snowflake bounding volume correspond to normalized surface-area-to-volume ratios of $\xi = 1,\ 3,\ 5$, respectively.

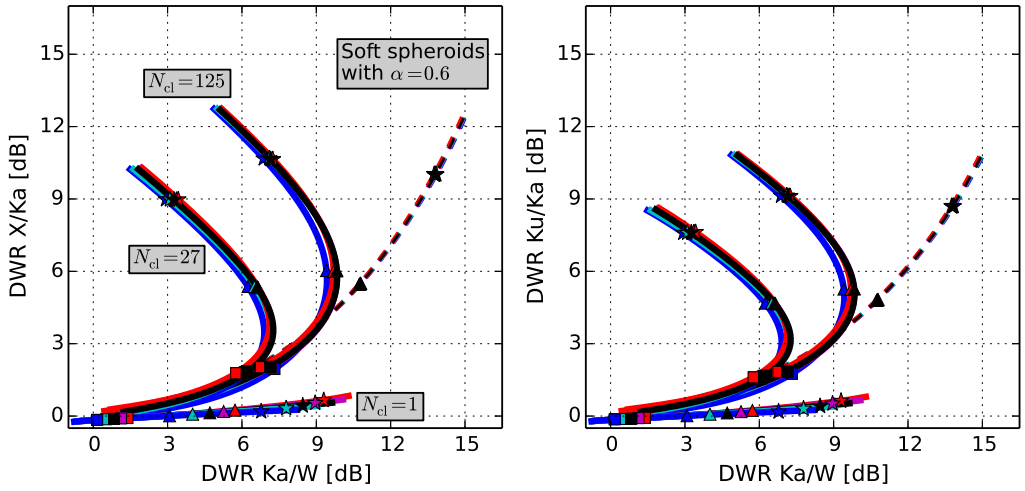

Figure S11. Modeled snowfall triple-frequency radar signatures as in Fig. S10, but derived for exponential size distributions limited to snowflake diameters of $D \leq D_{\max} = 10.0$ mm.

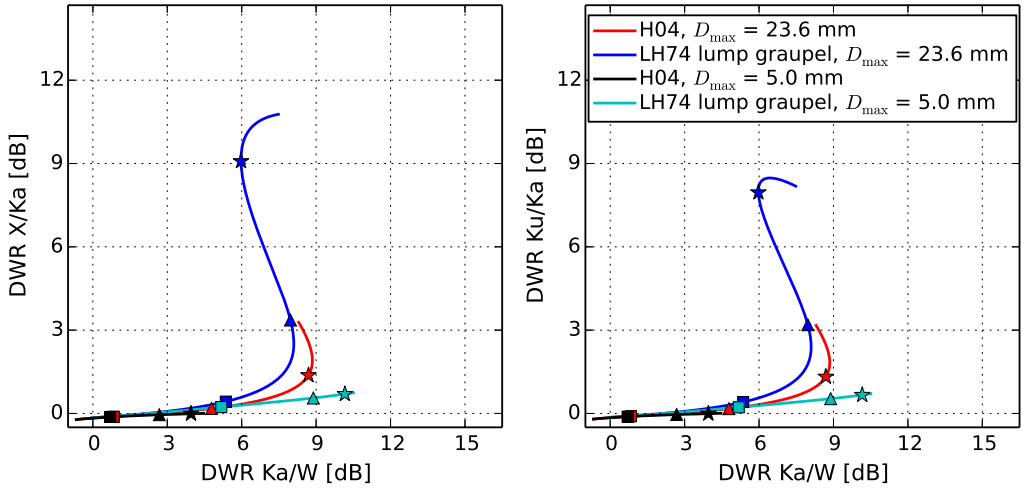

Figure S12. Comparison of modeled snowfall triple-frequency radar signatures determined for the H04 snowflake density–diameter relationship with modeled snowfall triple-frequency radar signatures determined for a snowflake mass–diameter relationship of $m_f(D) = 0.078D^{2.8}$ [m_f in mg, D in mm] which was derived by Locatelli and Hobbs (1974, LH74) to describe (dense) lump graupel, calculated for a normalized snowflake surface-area-to-volume ratio of $\xi = 1$ ($N_{cl} = 1$) and for exponential size distributions with snowflake diameters of $D \leq D_{\max}$.

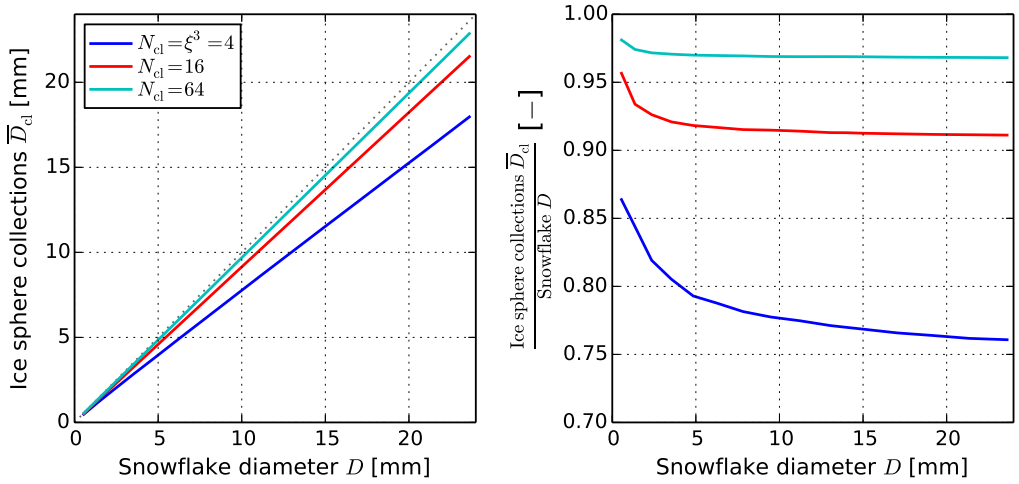

Figure S13. Relation between snowflake diameter D and the mean diameter $\overline{D}_{\rm cl}$ of 500 mass- and SAV-equivalent collections of randomly distributed ice spheres inside a spherical bounding volume of diameter D, determined for collections of $N_{\rm cl} = \xi^3 = 4,\ 16,\ 64$ ice spheres.

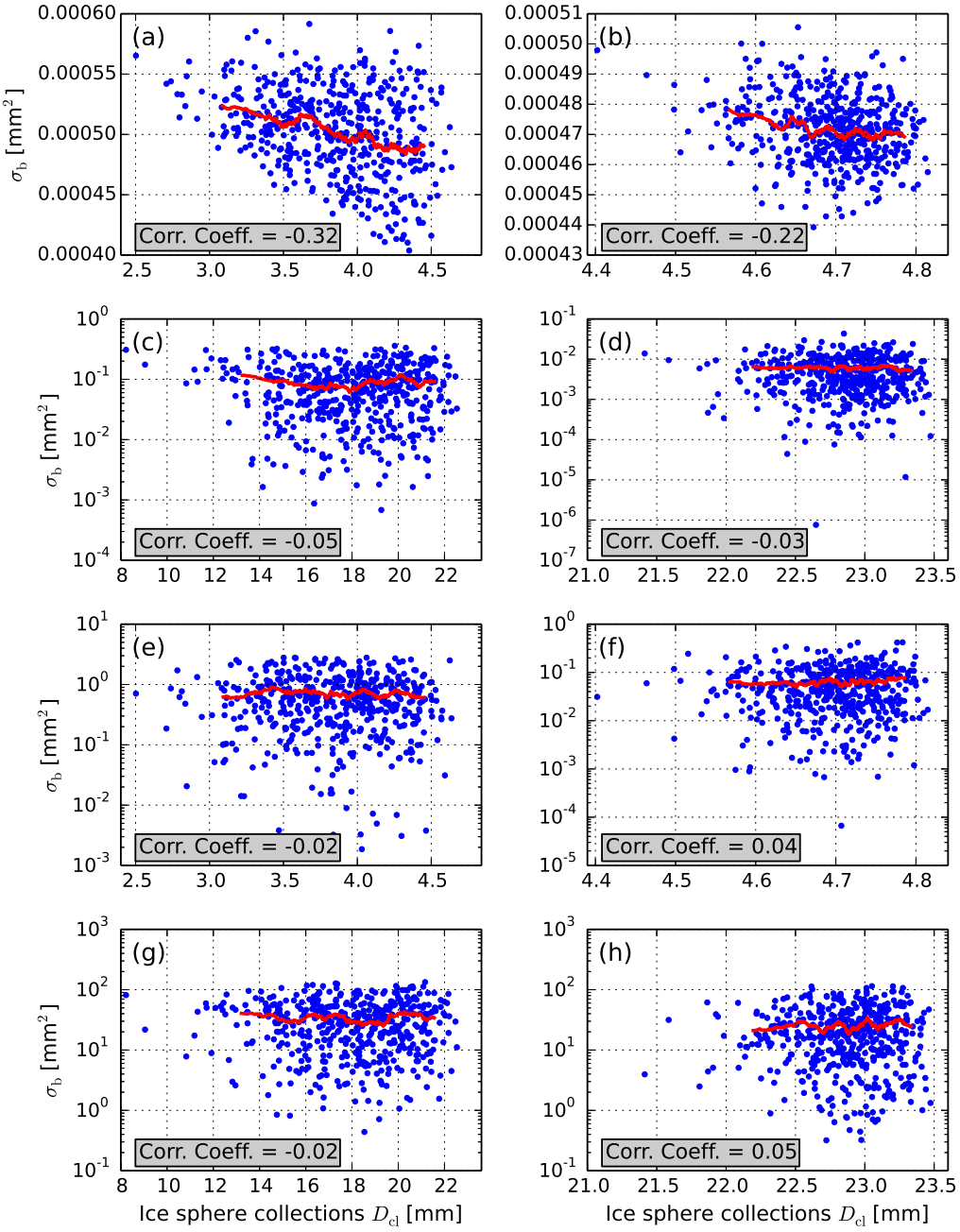

Figure S14. Illustration of the (weak) correlation between the calculated backscatter cross section σ_b for collections of randomly distributed ice spheres inside a spherical bounding volume of diameter D ($D =$ x-axis limit in each plot, 500 ice sphere collections per plot) and the diameter D_{cl} of the generated ice sphere collections. (a)–(d) 10 GHz, (e)–(h) 94 GHz; (a,e) $D = 4.84$ mm, $N_{cl} = \xi^3 = 4$; (b,f) $D = 4.84$ mm, $N_{cl} = \xi^3 = 64$; (c,g) $D = 23.6$ mm, $N_{cl} = 4$; (d,h) $D = 23.6$ mm, $N_{cl} = 64$. Gray boxes indicate the corresponding (linear) correlation coefficients and red lines show moving means calculated for subsets of 50 ice sphere collections.

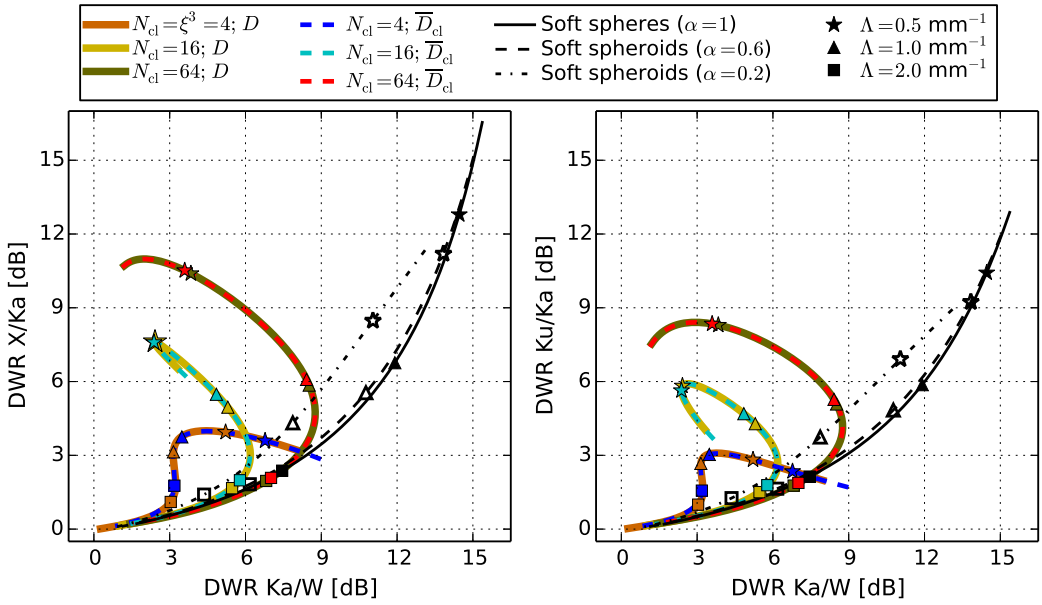

Figure S15. Influence of the choice of diameter (D vs. $\overline{D}_{\rm cl}$) on snowfall triple-frequency radar signatures modeled according to Sect. 3.4 for exponential size distributions with snowflake diameters of $D \leq D_{\rm max} = 23.6$ mm and exponential slope parameters of $0.3 \leq \Lambda \leq 5.0$ mm^{-1}. Solid colored lines show triple-frequency curves derived for collections of $N_{\rm cl} = \xi^3 = 4,\ 16,\ 64$ ice spheres when snowflake diameter D is used in Eq. (10), which is done throughout this study. Dashed colored lines indicate the corresponding triple-frequency curves when the mean diameter $\overline{D}_{\rm cl}$ of the generated ice sphere collections is used in Eq. (10) instead of D.

References

Heymsfield, A. J., Bansemer, A., Schmitt, C., Twohy, C., and Poellot, M. R.: Effective ice particle densities derived from aircraft data, J. Atmos. Sci., 61, 982–1003, 2004.

Hogan, R. J., Honeyager, R., Tyynelä, J., and Kneifel, S.: Calculating the millimetre-wave scattering phase function of snowflakes using the self-similar Rayleigh–Gans Approximation, Q. J. R. Meteorol. Soc., 143, 834–844, doi:10.1002/qj.2968, 2017.

Kneifel, S., von Lerber, A., Tiira, J., Moisseev, D., Kollias, P., and Leinonen, J.: Observed relations between snowfall microphysics and triple-frequency radar measurements, J. Geophys. Res. Atmos., 120, 6034–6055, doi:10.1002/2015JD023156, 2015.

Leinonen, J. and Szyrmer, W.: Radar signatures of snowflake riming: A modeling study, Earth Space Sci., 2, 346–358, doi:10.1002/2015EA000102, 2015.

Locatelli, J. D. and Hobbs, P. V.: Fall speeds and masses of solid precipitation particles, J. Geophys. Res., 79, 2185–2197, 1974.